AGU PUBLICATIONS

Geophysical Research Letters

Key Points:
- Space-weighted seismic attenuation mapping reconstructs the sources of the major monitored unrest at Campi Flegrei caldera
- High attenuation and seismicity highlight structurally controlled fluid migration and the two main zones of hydrothermal hazard
- Low attenuation at high frequencies supports the presence of an aseismic ancient/active magma body offshore Pozzuoli

Space-weighted seismic attenuation mapping of the aseismic source of Campi Flegrei 1983–1984 unrest

L. De Siena[1] **, A. Amoruso**[2] **, E. Del Pezzo**[3,4] **, Z. Wakeford**[1] **, M. Castellano**[3] **, and L. Crescentini**[5]

[1] School of Geosciences, Geology and Petroleum Geology, King's College, University of Aberdeen, Aberdeen, UK, [2] Dipartimento di Chimica e Biologia, Università degli Studi di Salerno, Fisciano, Italy, [3] Istituto Nazionale di Geofisica e Vulcanologia, Sezione di Napoli-Osservatorio Vesuviano, Naples, Italy, [4] Istituto Andalùz de Geofisica, Università de Granada, Granada, Spain, [5] Dipartimento di Fisica E. R. Caianiello, Università degli Studi di Salerno, Fisciano, Italy

Abstract Coda wave attenuation imaging is able to detect fluid/melt accumulation and ancient magmatic bodies in volcanoes. Here we use recently developed space-weighting sensitivity functions to invert for the spatial distributions of multifrequency coda wave attenuation (Q_c^{-1}), measured during the largest monitored unrest at Campi Flegrei caldera (1983–1984). High-attenuation anomalies are spatially correlated with the regions of highest structural complexities and cross faulting. They characterize deep fluid circulation in and around the aseismic roots of the 1534 A.D. Mount Nuovo eruption and fluid accumulation in the areas of highest hydrothermal hazard. Just offshore Pozzuoli, and at the highest frequency (wavelengths of ~150 m), the main cause of ground deformation and seismicity during the unrest is an aseismic low-attenuation circular anomaly, similar in shape and nature to those produced by ancient magmatic reservoirs and active sills at other volcanoes.

1. Introduction

Unrest episodes at volcanic calderas provide ideal geophysical, geological, and geochemical data sets to test advanced imaging methodologies, especially those employing the stochastic signature of highly heterogeneous materials on seismic waves [*Del Pezzo*, 2008; *Sato et al.*, 2012]. Campi Flegrei caldera (Italy; Figure 1a) has experienced long, monitored high-seismicity and high-deformation unrest episodes, which have given deep geophysical insight into the structural changes of its shallowest volcanic systems. In particular, the passive seismicity recorded onshore during its 1983–1984 unrest [e.g., *Aster et al.*, 1989] has been extensively used to model structures between depths of 0.5 and 4 km tomographically [*De Lorenzo et al.*, 2001; *Vanorio et al.*, 2005; *De Siena et al.*, 2010, 2011].

When compared with deformation measurements, this seismicity highlights inputs of magmatic fluids into the upper crustal systems [*D'Auria et al.*, 2011]. The accumulation of fluids in rocks additionally increases the pore pressure within the medium, reducing its effective normal stress and resistance to fracture [*Chiodini et al.*, 2010]. There is general disagreement regarding the nature (fluid, gaseous, or magmatic) of a 3–4 km deep high-attenuation [*De Siena et al.*, 2010], high-density [*Amoruso et al.*, 2008], low $\frac{V_P}{V_S}$ [*Vanorio et al.*, 2005] seismic volume located under Pozzuoli (**P**, Figures 1a–1c). This is the main source of deformation during past and recent unrests [*Battaglia et al.*, 2006; *Amoruso et al.*, 2008; *Woo and Kilburn*, 2010; *Amoruso et al.*, 2014a, 2014b; *Di Vito et al.*, 2016], producing ground uplift of ~1.8 m during the 1983–1984 unrest [*Del Gaudio et al.*, 2010]. Nevertheless, scientists generally agree that a stable hydrothermal reservoir permeates the upper 3 km of the caldera, feeds on meteoric and deep magmatic sources, and responds to caldera unrests [e.g., *De Siena et al.*, 2010; *Chiodini et al.*, 2010; *D'Auria et al.*, 2011; *Petrillo et al.*, 2013]. While much geophysical information related to hydrothermal activity is available onshore, only recently the scientific community has focused on the offshore structures [*Capuano et al.*, 2013; *Carlino et al.*, 2016]. These feed fumarole centers, are affected by coastal shape and bathymetry [*Vilardo et al.*, 2013; *Petrillo et al.*, 2013], and were exploited by AGIP (a giant Italian energy retailer) in the last century. Differences between the 2005–2014 and 1982–1984 seismic focal volumes suggest changes in medium response during the last 35 years. *Di Luccio et al.* [2015] observe a transition from an elastic to a plastic behavior following the 1982–1984 crisis and attribute it to fluid saturation and
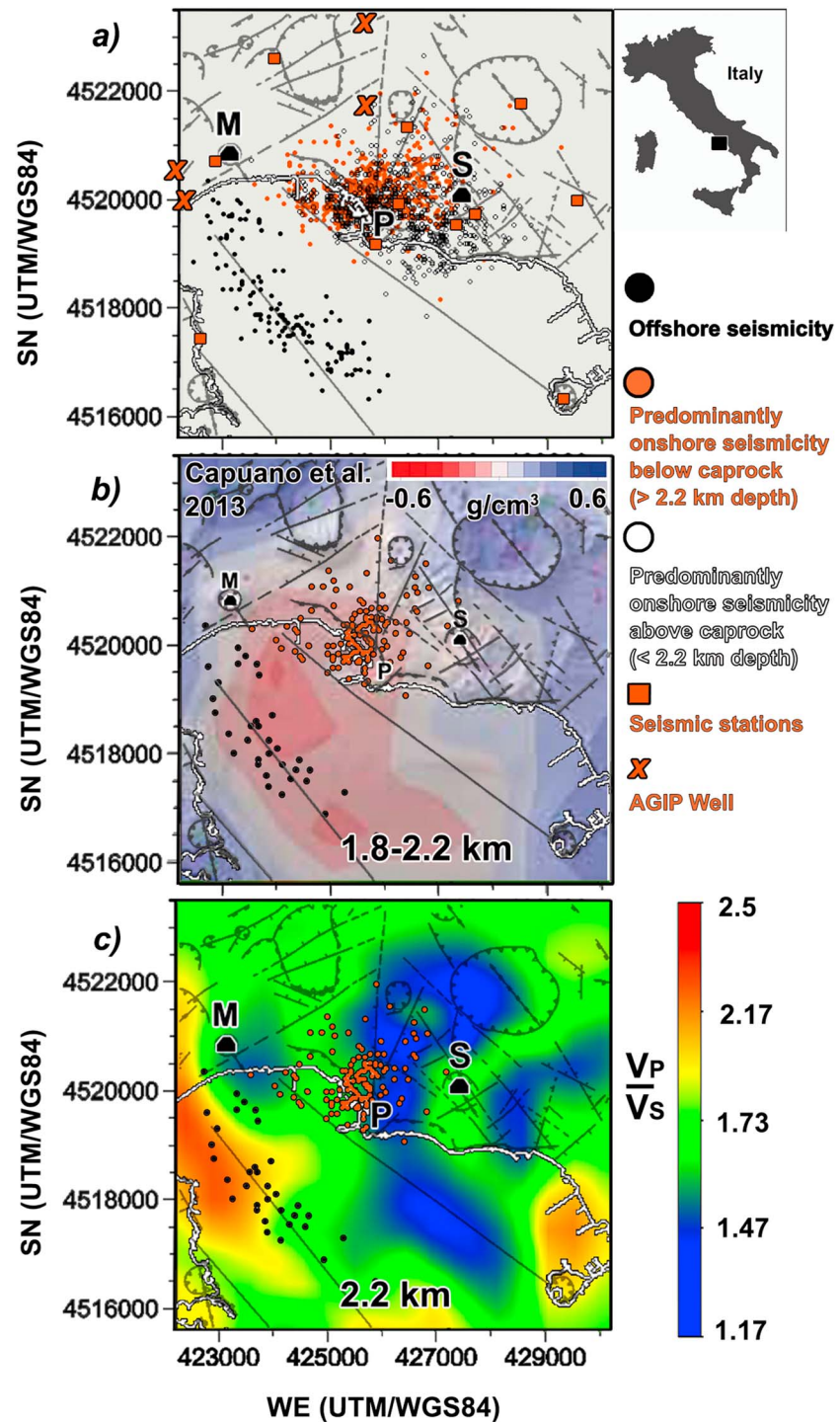
Figure 1. Seismicity, geomorphology, gravimetry, and $\frac{V_P}{V_S}$. (a) Relocalized seismic patters produced by the 1983–1984 seismic unrest of Campi Flegrei. Open circles and orange circles represent onshore seismicity above and below the caprock bottom (2.2 km) as defined by rock physics experiments [*Vanorio and Kanitpanyacharoen*, 2015]. Black circles show the offshore seismicity at all depths. Geomorphology and known offshore faults are superimposed (gray lines; see *Vilardo et al.* [2013]). Mount Nuovo (**M**), Pozzuoli (**P**), and Solfatara (**S**) volcanic centers are drawn on geomorphology. AGIP deep wells are marked by several orange crosses. On the right we show the location of Campi Flegrei in Italy. (b) Gravimetric deviations at Campi Flegrei between 1.8 and 2.2 km depth taken from *Capuano et al.* [2013]. Seismicity at the corresponding depths is superimposed. (c) $\frac{V_P}{V_S}$ measurements redrawn from *Vanorio et al.* [2005] with seismicity superimposed.
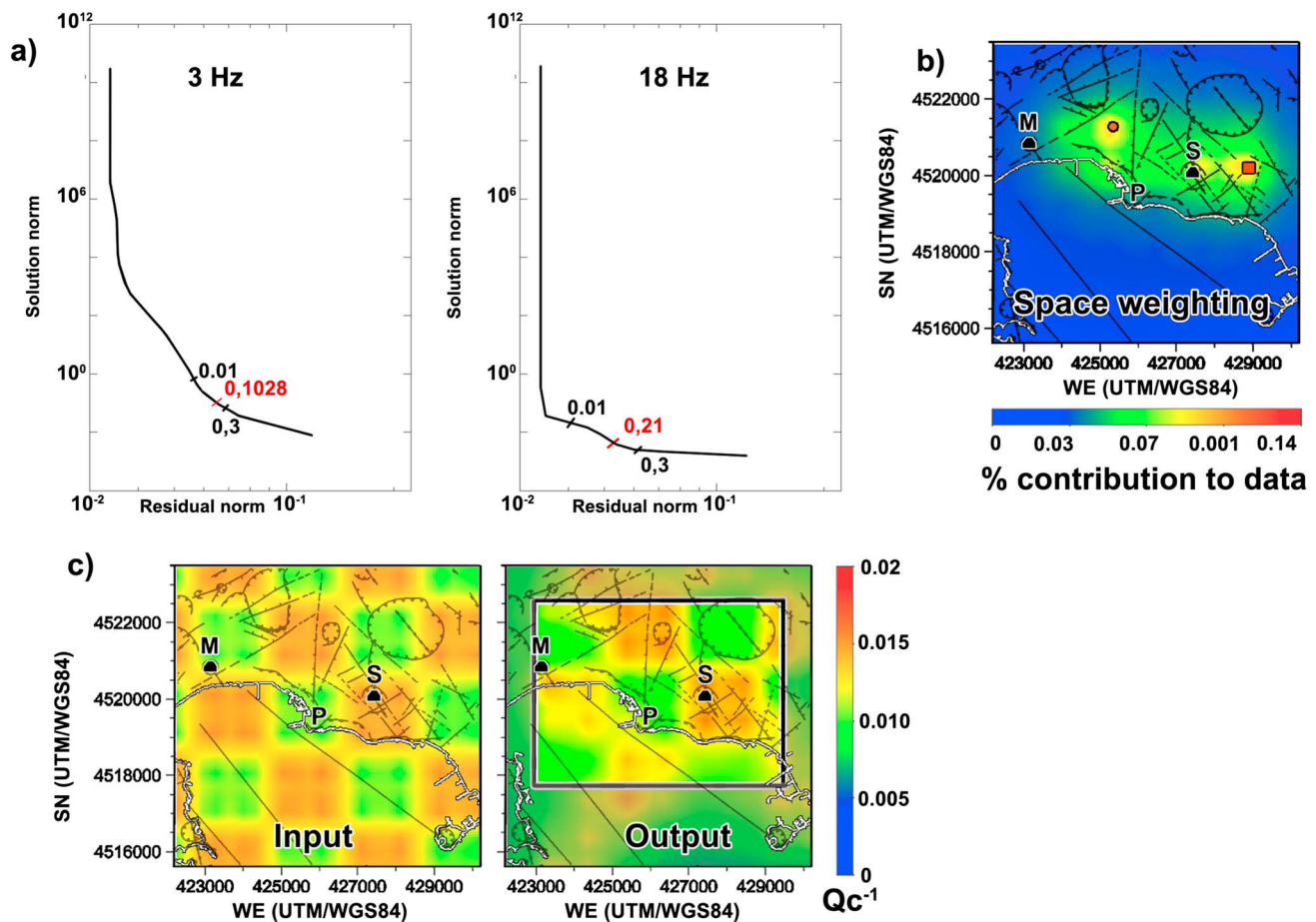
Figure 2. Damping, sensitivity, and resolution. (a) *L* curves with chosen optimal damping parameters (red) for the linear inversions at 3 Hz and 18 Hz. (b) The space-weighting function is represented as the percentage contribution of each node to the coda quality factor measurement for a single source (orange circle)-receiver (orange square) pair. (c) The checkerboard test uses 2×2 km cells (left, input; center, output). The thick black line is drawn considering the values and shapes of the Q_c^{-1} anomalies in the output. It contours the areas discussed in the main text.

heating of the rocks in the hydrothermal reservoir. In particular, the 2012–2014 deeper earthquakes are located in a low $\frac{V_P}{V_S}$ zone at the western boundary of the hydrothermal reservoir.

A reliable onshore and offshore seismic mapping of attenuation, absorption, and scattering gives deeper insight into fluid/melt accumulation in volcanic and geothermal areas [*Prudencio et al.*, 2015a; *De Siena et al.*, 2016]. Such a frequency-dependent mapping can be obtained via integrated measurements of peak delay and coda quality factor (Q_c), as done at Mount St. Helens volcano [*De Siena et al.*, 2016]. Mapping Q_c using appropriate sensitivity space-weighting functions [*Prudencio et al.*, 2013; *Del Pezzo et al.*, 2016] provides a direct measurement of absorption in a quasi-diffusive regime. If the actual regime is not diffusive (due to, e.g., resonance or surface wave contamination [*De Siena et al.*, 2013; *Mayor et al.*, 2016]), Q_c is a nonlinear combination of anisotropy, scattering, and intrinsic attenuation and Q_c^{-1} can only be defined broadly as coda wave attenuation [*Sato et al.*, 2012]. At Campi Flegrei, seismic envelopes show a diffusive behavior for epicentral distances greater than 2 km [*De Siena et al.*, 2013]; hence, attenuation space-weighting functions devised for diffusive media, as those defined by *Del Pezzo et al.* [2016], may be used to model coda attenuation, providing more precise lateral imaging with respect to ray-dependent techniques.

We propose a novel frequency-dependent coda attenuation mapping based on space-weighting functions at Campi Flegrei caldera. This is integrated by averaged over time relocated seismicity recorded during the 1983–1984 volcanic unrest. The objective is to locate and model in space the sources of high fumarolic activity, ground deformation, and hydrothermal activity during the unrest [*Todesco et al.*, 2010; *Chiodini et al.*, 2010; *Amoruso et al.*, 2014a]. The increased lateral illumination with respect to standard Q_c imaging may lead
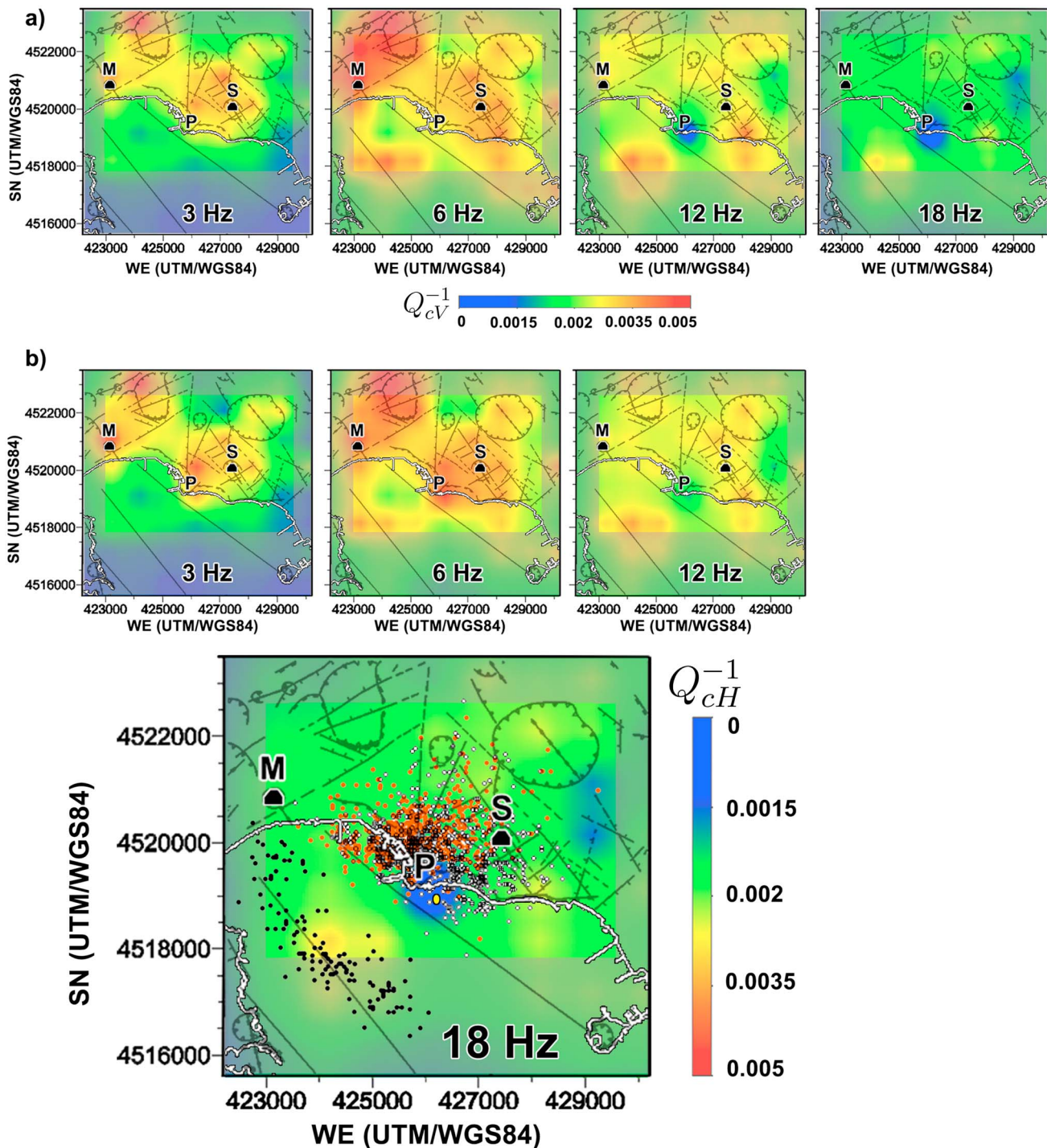
Figure 3. Coda attenuation mapping obtained using (a) vertical (Q_{cV}^{-1}) and (b) horizontal (Q_{cH}^{-1}) components of motions. A grey mask shades unresolved anomalies. The seismicity of Figure 1a is imposed on the 18 Hz horizontal image.

to better understanding of the feeding mechanisms active at the volcano at present and historical times [*Todesco et al.*, 2014; *Di Napoli et al.*, 2016; *Di Vito et al.*, 2016], as done at other volcanoes [*Prudencio et al.*, 2015a, 2015b]. The study thus gives a different seismic imaging perspective on the problem of locating deformation and unrest sources related to hydrothermal dynamics. Understanding the mechanisms and extension of fluid migration/accumulation is crucial for exploiting the derived geothermal energy [*Piochi et al.*, 2014; *Carlino et al.*, 2016], evaluating volcanic and hydrothermal hazard in the region [*Selva et al.*, 2012;

Bevilacqua et al., 2015], and testing the feasibility of mechanisms producing subsidence and uplift during the last two millennia [*Todesco et al.*, 2014; *Vanorio and Kanitpanyacharoen*, 2015; *Di Vito et al.*, 2016].

2. Data and Methods

2.1. Microearthquakes

We relocalize the seismicity recorded in 1983–1984 at Campi Flegrei caldera by using the NonLinLoc software [*Lomax et al.*, 2001] and the 3-D *P* and *S* wave velocity models of *Battaglia et al.* [2008], which integrate the unrest seismicity with recordings of an active survey offshore Pozzuoli. The seismic data set comprises a total of >200,000 *P* and *S* wave pickings, corresponding to 1361 microearthquakes (Figure 1a). The pickings have been measured on waveforms recorded from January 1983 to December 1984 by the combined permanent analog networks of the Osservatorio Vesuviano and Aquater Agip (20 stations [see *Vanorio et al.*, 2005; *Piochi et al.*, 2014]). Additional pickings have been measured on the high-quality waveform data set recorded by a temporary array of 15 three-component digital stations, installed by the University of Wisconsin between January and April 1984 [*Aster et al.*, 1989]. The microearthquakes are selected requiring a minimum of eight *P* phases or six *P* phases and two *S* phases. All events have a root-mean-square error lower than 0.3 s, leading to average spatial uncertainties of less than 0.3 km, and a single maximum in the complete nonlinear localization probability for each event [*Lomax et al.*, 2001]. Microseismicity depths range from 0.5 to 4.5 km.

While the 2 year long areal microseismic patterns agree with those recently obtained by *Di Luccio et al.* [2015], the use of a 3-D velocity model in the grid search algorithm allows for the inclusion of the temporary stations of the University of Wisconsin. The main difference with respect to previous localizations are an increase in the number of locations, particularly offshore, and a better contour of offshore seismic faults (Figure 1a, black dots; geomorphology from *Vilardo et al.* [2013]) bounding an aseismic zone located SW of the city of Pozzuoli just south of Mount Nuovo (Figure 1a). Open circles (seismicity above 2.2 km) connect Pozzuoli and Solfatara, while deeper (orange) seismicity ranges between Pozzuoli and the San Vito-Astroni geothermal field. The offshore seismic region coincides with a bathymetric low and is embedded into the southeastern undeformed-to-subsiding portion of the Pozzuoli Bay, separated by northeastern shallower resurgent portion of the caldera [*Capuano et al.*, 2013]. The area is spatially correlated with a relevant gravimetric low at all depths down to 2.2 km (Figure 1b reproduces Figure 4 in *Capuano et al.* [2013]) near the most relevant high in $\frac{V_P}{V_S}$ (of the order of 2.5) between depths of 2 and 3 km (Figure 1c) [see *Vanorio et al.*, 2005].

2.2. Inversion of 2-D Attenuation Parameters

We map coda wave attenuation via multifrequency (*f*) *S* wave coda quality factor (Q_c) measurements using the high-quality three-component data set of seismic waveforms recorded between January and April 1984 by the University of Wisconsin temporary array. *De Siena et al.* [2010] extensively describe the data set of 2559 waveforms corresponding to the strongest seismic unrest. The same data set is used in *De Siena et al.* [2013] to demonstrate that diffusion laws model seismic envelopes during the unrest for epicentral distances (*D*) greater than 2 km—the minimum distance in the present study.

We use the 2-D attenuation space-weighting functions defined by *Del Pezzo et al.* [2016] for each source of coordinate $[x_s, y_s]$ and receiver $[x_r, y_r]$ pair (Figure 2b), in order to map the effective sensitivity of the Q_c parameters in space (x, y) and build the rows of the inversion matrix. The weighting functions are computed via a Monte Carlo numerical simulation of the Energy Transport Equation in a diffusive highly heterogeneous medium. Both absorption and scattering attenuation mechanisms result in similar space-weighting functions. Space-weighted attenuation functions are thus applied as an approximated analytical sensitivity function for source-receiver 2-D Q_c mapping (see *Del Pezzo et al.* [2016] for details about the construction of the weighting functions):

$$f[x, y, x_r, y_r, x_s, y_s] = \frac{1}{4\pi\delta_x D^2 \delta_y} \exp\left[-\frac{\left(x - \frac{x_r + x_s}{2}\right)^2}{2\left(\delta_x D\right)^2} + \frac{\left(y - \frac{y_r + y_s}{2}\right)^2}{0.5\left(\delta_y D\right)^2} \right]$$

$$+ \frac{1}{2\pi\delta_x D^2 \delta_y} \exp\left[-\frac{\left(x - x_s\right)^2}{2\left(\delta_x D\right)^2} + \frac{\left(y - y_s\right)^2}{2\left(\delta_y D\right)^2} \right]$$

$$+ \frac{1}{2\pi\delta_x D^2 \delta_y} \exp\left[-\frac{\left(x - x_r\right)^2}{2\left(\delta_x D\right)^2} + \frac{\left(y - y_r\right)^2}{2\left(\delta_y D\right)^2} \right] \quad (1)$$

The spatial apertures of the weighting functions (δ_x and δ_y) are set to 0.2 due to the fitting between analytical and computational functions, observed by *Del Pezzo et al.* [2016]. We use these functions to set the contribution of the nodes of a 2-D, 0.5 km spaced map comprising the entire Campi Flegrei caldera (the area in Figures 1–3) to each source-receiver Q_c measurement for the lapse times modeled by the functions. Each measurement is thus taken by modeling the first 20 s of the *S* wave smoothed envelope [*Del Pezzo et al.*, 2016] after filtering in four frequency bands, centered at 3 Hz, 6 Hz, 12 Hz, and 18 Hz, and with bandwith one third of the central frequency. The weighting functions provide the rows of the inversion matrix at the nodes after normalization for the total weight relative to the source-receiver pair: the main assumption is that total coda attenuation (summing to 1) is caused by the medium comprising the inversion grid. The data vector for each source-receiver pair is the total inverse Q_c measurement: we obtain four data vectors after filtering in the above-mentioned frequency bands. The model parameters are the inverse Q_c at each node and are obtained at each frequency by a first-order Tikhonov inversion [e.g., *De Siena et al.*, 2010]. In Figure 2a, we show the *L* curves corresponding to the inversions at 3 Hz and 18 Hz, with the chosen optimal damping parameters (red).

2.3. Synthetic Tests

In Figure 2b, a sample 2-D coda attenuation normalized weighting function is computed for a source-receiver pair. The space-weighted functions increase lateral illumination with respect to ray-dependent measurements. The contribution of all nodes of the grid to the single-station Q_c^{-1} measurement is plotted by using a color scale, with the values in the color bar showing the coefficients of the corresponding row of the inversion matrix. The effective resolution of our images is estimated via a checkerboard test with cell dimension 4 times the node spacing (2 km, Figure 2c). The procedure is identical to that described by *De Siena et al.* [2010] for a 3-D body wave total attenuation inversion. The black rectangle contours the resolved area. The resolved anomalies retain most of their attenuation potential, with major damping across the caldera border. In Figures 3a and 3b we shade the areas of poor or no resolution with a grey mask.

Any discrepancy with respect to the diffusive model (multiple scattering), particularly the anisotropy of scattering affecting early coda waves, will result in biases within the computed space-weighting functions and corresponding images [*Mayor et al.*, 2016]. These differences will produce different effects on maps obtained using horizontal and vertical components. Therefore, we compare coda attenuation maps obtained using vertical (Figure 3a, Q_{cV}^{-1}) and horizontal (Figure 3b, Q_{cH}^{-1}, obtained by averaging the West-East (WE) and South-North (SN) Q_c values at each node) components of motions. The two images are basically identical at the investigated resolution, and only horizontal images will be further discussed (Figure 3b). The test is indicative of the fact that equipartition is fulfilled and our assumptions are valid at the lapse times considered [*Calvet and Margerin*, 2013].

3. Results and Discussions

3.1. High-Attenuation Anomalies: Correlation With Geomorphological Heterogeneity, Hydrogeothermal Resources, and Hazards

Q_c mapping at both regional [*Mayor et al.*, 2016] and local volcanic [*De Siena et al.*, 2016] scales shows that higher-frequency maps (12–18 Hz) are more sensitive to deeper Earth layers than low frequencies (3–6 Hz). Geological features such as extensional basins, crustal high-density bodies, and debris flows can be reconstructed by low-frequency mapping, mainly as a consequence of surface wave contamination. An extreme case is Mount St. Helens volcano, where the highly heterogeneous tens of meters thick pyroclastic flow layers produced by the 1980 eruption, reconstructed by means of GIS and InSAR, is modeled using 3 Hz Q_c and peak delay mapping [*De Siena et al.*, 2016]. In the following discussion, we will therefore assume that depth increases with frequency, as originally postulated by *Aki and Chouet* [1975]. At Campi Flegrei, low-frequency high-attenuation anomalies characterize surface fractured areas, specifically those presenting cross faulting, independently of seismic and deformation activity [*Vilardo et al.*, 2013; *Piochi et al.*, 2014]. At 3 Hz (Figure 3b) high attenuation in fact marks extensive cross faulting (1) in the onshore seismic zone between Pozzuoli and Solfatara (**P** and **S**, Figures 1–3) and (2) the aseismic regions north of Mount Nuovo (**M**). The Pozzuoli-Solfatara anomaly coincides with the area of highest seismic clustering (Figure 1a), high shallow $\frac{V_P}{V_S}$, high body wave attenuation, and a 3–4 km deep high-gravity anomaly [*Vanorio et al.*, 2005; *Amoruso et al.*, 2008; *De Siena et al.*, 2010]. Moreover, it borders the offshore region of maximum deformation [e.g., *Amoruso et al.*, 2014a]. On the contrary, the area north of Mount Nuovo is aseismic and characterized by average $\frac{V_P}{V_S}$ and gravimetric anomalies (Figures 1a–1c).

Increasing frequency to 6 Hz (Figure 3b), the Pozzuoli-Solfatara anomaly expands east toward Astroni and Agnano, while the Mount Nuovo anomaly extends offshore. The extension offshore Mount Nuovo (1) coincides with the area of maximum seismic scattering attenuation [*De Siena et al.*, 2011], (2) is spatially correlated with the only high $\frac{V_P}{V_S}$ anomaly at 2.2 km depth (Figure 1c), and (3) is seismically active (Figure 1a). In our interpretation, it is thus the attenuation signature of hydrothermal fluids migrating through fractures and faults [*Piochi et al.*, 2014] and today mixed with meteoric waters [*Petrillo et al.*, 2013] offshore Mount Nuovo. The same volumes are today visible as the densely fractured, fluid-saturated buried rim of the caldera down to 1 km depth [*Serlenga et al.*, 2016]. Seismicity shows how fluids migrate from the caldera center, entering the Campi Flegrei upper hydrothermal systems in 1984 [*Battaglia et al.*, 2006; *Petrillo et al.*, 2013]. Increasing frequency, the anomaly follows the strike of the seismic offshore caldera-bounding faults and is stronger in the center of the low-gravity subsiding part of the caldera (see Figure 3b, 12 Hz and 18 Hz [*Capuano et al.*, 2013]). The upward fluid migration is thus restricted to structurally controlled pathways [*D'Auria et al.*, 2011] and stops at vents active during the last 5000 years east of Pozzuoli [*Vilardo et al.*, 2013].

High-attenuation anomalies at 6–18 Hz (Figure 3b) are the seismic signature of the processes leading to accumulation of geothermal fluids, extracted by onshore AGIP wells (Figure 1a, orange x) [see *Vanorio et al.*, 2005; *Piochi et al.*, 2014]. The 2 year long circular shallow seismicity south of Mount Nuovo corresponds to high $\frac{V_P}{V_S}$ (Figure 1b) and is feasibly the seismic signature of the pressure drop within the hydrothermal system, following the changes in permeability caused by injection of either magma [*Amoruso et al.*, 2008] or fluids [*D'Auria et al.*, 2011] under Pozzuoli. These structurally controlled seismic paths are direct evidence of changes in permeability induced by fluid migrations [*Battaglia et al.*, 2006], a mechanism inducing subsidence in the years following the unrest [*Del Gaudio et al.*, 2010], and particularly effective in the offshore SW portion of the caldera in recent and historical unrests [*Todesco et al.*, 2014].

Deep seismic patterns (Figure 1a, orange dots) show a progressive shift from Pozzuoli (where the injection of magma and/or fluid is modeled by different authors [*Amoruso et al.*, 2008; *D'Auria et al.*, 2011] to north of Solfatara (San Vito-Agnano). They cross the region of main geomorphological heterogeneity (Figure 1a) and highest degassing [*Chiodini et al.*, 2010]. At all frequencies up to 12 Hz, Pozzuoli-Solfatara is stably the region of highest attenuation. The Agnano-San Vito area coincides with the region of highest probability for future vent openings [*Selva et al.*, 2012; *Bevilacqua et al.*, 2015]. The 18 Hz high-attenuation anomaly offshore Mount Nuovo is instead spatially correlated with the second most likely region of vent opening [*Selva et al.*, 2012]. Once integrated by density and $\frac{V_P}{V_S}$ measurements, the nature and depths of these two reservoirs appear different, although still clearly connected with the availability of deep geothermal resources (Figure 1a). Attenuation mapping thus clearly highlights the hazardous potential of both areas, which, from our analysis, could take the form of future hydrothermal explosions.

3.2. Low-Attenuation Anomalies: Mapping the Source of Campi Flegrei Unrest

The main low-attenuation anomaly at 18 Hz is aseismic and encompasses the center of the area of maximum uplift, even considering its maximum uncertainties [*Amoruso et al.*, 2014a, 2014b] (Figure 3b, 18 Hz, yellow elliptic area). A similar high-frequency, low-attenuation anomaly marks the location of the deep magma conduits feeding Mount St. Helens volcano [*De Siena et al.*, 2016]. Seismic attenuation tomography using coda-normalized direct energies at Tenerife Island reveals that low-attenuation anomalies are related to the position of potential ancient magma reservoirs [*Prudencio et al.*, 2015b]. As shown by *Di Vito et al.* [2016] using the historical, archeological, and geological record of Campi Flegrei caldera, progressive magma accumulation has been acting under the caldera center in a 4.6 ± 0.9 km deep source. This pattern is consistent with the deformation source shown in Figure 3b (18 Hz) [*Amoruso et al.*, 2014a]. The authors also demonstrate transfer to a 3.8 ± 0.6 km deep magmatic source ∼4 km NW of the caldera center, below Mount Nuovo, compatible with our previous discussion. In our interpretation, this repeated emplacement of magma through intrusions below the caldera center is the cause of the 18 Hz coda attenuation image and seismic patterns (Figure 3b, 18 Hz). Our resolution does not allow to reconstruct eventual active sills thinner than 500 m in the 0 to 4.5 km depth range, which could better fit deformation, remote sensing, and gravimetry results [*Amoruso et al.*, 2008, 2014a].

4. Conclusions

In volcanic media, coda wave attenuation mapping and microearthquake locations better constrain fluid and gas accumulation with respect to deterministic traveltime tomography, using much smaller data sets.

At Campi Flegrei, the approach highlights the importance of the boundary between resurgent and subsiding portions of the caldera, as well as structural paths in enhancing fluid migration and accumulation. The study marks the two main high-attenuation zones where geothermal resources accumulate. The first is a fluid-bearing reservoir in the SW submerged portion of the caldera, connected with the subsidence mechanisms acting near Mount Nuovo and following the 1983–1984 unrest. The second fluid-bearing reservoir feeds local fumarole fields in the resurgent NE onshore portion of the caldera. While the potential in exploration settings using active seismicity is self-evident, the spatial correlation with the two areas of highest probability for vent opening highlights the potential of the technique in routine hazard assessment of volcanic areas.

The most important anomaly in our results is a low-attenuation circular area, enclosing the area of maximum deformation during unrest. This aseismic region has the same characteristics of active and extinct magmatic chambers/sills at other volcanoes and is contoured by most of the 1–4.5 km deep seismicity during the unrest. It is thus interpreted as either extinct magmatic materials, acting as caprock for a deeper source of unrest, or an active magmatic source. Additional interdisciplinary constraints and improved 3-D interdisciplinary imaging are necessary to better define the shape and nature of the structure.

References

Aki, K., and B. Chouet (1975), Origin of coda waves: Source, attenuation, and scattering effects, *J. Geophys. Res.*, *80*, 3322–3342.

Amoruso, A., L. Crescentini, and G. Berrino (2008), Simultaneous inversion of deformation and gravity changes in a horizontally layered half-space: Evidences for magma intrusion during the 1982–1984 unrest at Campi Flegrei caldera (Italy), *Earth Planet. Sci. Lett.*, *272*(1), 181–188.

Amoruso, A., L. Crescentini, and I. Sabbetta (2014a), Paired deformation sources of the Campi Flegrei caldera (Italy) required by recent (1980–2010) deformation history, *J. Geophys. Res. Solid Earth*, *119*, 858–879, doi:10.1002/2013JB010392.

Amoruso, A., L. Crescentini, I. Sabbetta, P. De Martino, F. Obrizzo, and U. Tammaro (2014b), Clues to the cause of the 2011–2013 Campi Flegrei caldera unrest, Italy, from continuous GPS data, *Geophys. Res. Lett.*, *41*, 3081–3088, doi:10.1002/2014GL059539.

Aster, R., R. Meyer, G. D. Natale, M. Martini, E. Del Pezzo, G. Iannaccone, and R. Scarpa (1989), Seismic investigation of the Campi Flegrei: A synthesis and summary of results, in *Volcanic Seismology, Proc. Volc. Series III*, edited by K. Aki, P. Gasparini, and R. Scarpa, pp. 462–483, Springer, San Francisco, Calif.

Battaglia, J., C. Troise, F. Obrizzo, F. Pingue, and G. D. Natale (2006), Evidence of fluid migration as the source of deformation at Campi Flegrei caldera (Italy), *Geophys. Res. Lett.*, *33*, L01307, doi:10.1029/2005GL024904.

Battaglia, J., A. Zollo, J. Virieux, and D. Dello Iacono (2008), Merging active and passive data sets in traveltime tomography: The case study of Campi Flegrei caldera (Southern Italy), *Geophys. Prospect.*, *56*, 555–573.

Bevilacqua, A., et al. (2015), Quantifying volcanic hazard at Campi Flegrei caldera (Italy) with uncertainty assessment: 1. Vent opening maps, *J. Geophys. Res. Solid Earth*, *120*, 2309–2329, doi:10.1002/2014JB011775.

Calvet, M., and L. Margerin (2013), Lapse time dependence of coda *Q*: Anisotropic multiple-scattering models and application to Pyrenees, *Bull. Seismol. Soc. Am.*, *103*(3), 1993–2010, doi:10.1785/0120120239.

Capuano, P., G. Russo, L. Civetta, G. Orsi, M. D'Antonio, and R. Moretti (2013), The active portion of the Campi Flegrei caldera structure imaged by 3-D inversion of gravity data, *Geochem. Geophys. Geosyst.*, *14*, 4681–4697, doi:10.1002/ggge.20276.

Carlino, S., A. Troiano, M. G. Di Giuseppe, A. Tramelli, C. Troise, R. Somma, and G. De Natale (2016), Exploitation of geothermal energy in active volcanic areas: A numerical modelling applied to high temperature Mofete geothermal field, at Campi Flegrei caldera (Southern Italy), *Renewable Energy*, *87*, 54–66.

Chiodini, G., S. Caliro, C. Cardellini, D. Granieri, R. Avino, A. Baldini, M. Donnini, and C. Minopoli (2010), Long-term variations of the Campi Flegrei, Italy, volcanic system as revealed by the monitoring of hydrothermal activity, *J. Geophys. Res.*, *115*, B03205, doi:10.1029/2008JB006258.

D'Auria, L., F. Giudicepietro, I. Aquino, G. Borriello, C. Del Gaudio, D. Lo Bascio, M. Martini, G. P. Ricciardi, P. Ricciolino, and C. Ricco (2011), Repeated fluid-transfer episodes as a mechanism for the recent dynamics of Campi Flegrei caldera (1989–2010), *J. Geophys. Res.*, *116*, B04313, doi:10.1029/2010JB007837.

De Lorenzo, S., A. Zollo, and F. Mongelli (2001), Source parameters and three-dimensional attenuation structure from the inversion of microearthquake pulse width data: Qp imaging and inferences on the thermal state of the Campi Flegrei caldera (southern Italy), *J. Geophys. Res.*, *106*, 16,265–16,286.

De Siena, L., E. Del Pezzo, and F. Bianco (2010), Seismic attenuation imaging of Campi Flegrei: Evidence of gas reservoirs, hydrothermal basins, and feeding systems, *J. Geophys. Res.*, *115*, B09312, doi:10.1029/2009JB006938.

De Siena, L., E. Del Pezzo, and F. Bianco (2011), A scattering image of Campi Flegrei from the autocorrelation functions of velocity tomograms, *Geophys. J. Int.*, *184*(3), 1304–1310.

De Siena, L., E. Del Pezzo, C. Thomas, A. Curtis, and L. Margerin (2013), Seismic energy envelopes in volcanic media: In need of boundary conditions, *Geophys. J. Int.*, *192*(1), 326–345.

De Siena, L., M. Calvet, K. J. Watson, A. Jonkers, and C. Thomas (2016), Seismic scattering and absorption mapping of debris flows, feeding paths, and tectonic units at Mount St. Helens volcano, *Earth Planet. Sci. Lett.*, *442*, 21–31.

Del Gaudio, C., I. Aquino, G. Ricciardi, C. Ricco, and R. Scandone (2010), Unrest episodes at Campi Flegrei: A reconstruction of vertical ground movements during 1905–2009, *J. Volcanol. Geotherm. Res.*, *195*(1), 48–56.

Del Pezzo, E. (2008), Seismic wave scattering in volcanoes, in *Earth Heterogeneity and Scattering Effects of Seismic Waves, Advances in Geophysics*, vol. 50, chap. 13, pp. 353–369, Elsevier, Amsterdam.

Del Pezzo, E., J. Ibañez, J. Prudencio, F. Bianco, and L. De Siena (2016), Absorption and scattering 2-D volcano images from numerically calculated space-weighting functions, *Geophys. J. Int.*, *206*(2), 742–756.

Di Luccio, F., N. Pino, A. Piscini, and G. Ventura (2015), Significance of the 1982–2014 Campi Flegrei seismicity: Preexisting structures, hydrothermal processes, and hazard assessment, *Geophys. Res. Lett.*, *42*, 7498–7506, doi:10.1002/2015GL064962.

Di Napoli, R., et al. (2016), Hydrothermal fluid venting in the offshore sector of Campi Flegrei caldera: A geochemical, geophysical, and volcanological study, *Geochem. Geophys. Geosyst.*, *17*, 4153–4178, doi:10.1002/2016GC006494.

Di Vito, M. A., et al. (2016), Magma transfer at Campi Flegrei caldera (Italy) before the 1538 AD eruption, *Sci. Rep.*, *6*, 32245, doi:10.1038/srep32245.

Lomax, A., A. Zollo, P. Capuano, and J. Virieux (2001), Precise, absolute earthquake location under Somma-Vesuvius volcano using a new three-dimensional velocity model, *Geophys. J. Int.*, *146*, 313–331.

Mayor, J., M. Calvet, L. Margerin, O. Vanderhaeghe, and P. Traversa (2016), Crustal structure of the Alps as seen by attenuation tomography, *Earth Planet. Sci. Lett.*, *439*, 71–80.

Petrillo, Z., G. Chiodini, A. Mangiacapra, S. Caliro, P. Capuano, G. Russo, C. Cardellini, and R. Avino (2013), Defining a 3D physical model for the hydrothermal circulation at Campi Flegrei caldera (Italy), *J. Volcanol. Geotherm. Res.*, *264*, 172–182.

Piochi, M., C. Kilburn, M. Di Vito, A. Mormone, A. Tramelli, C. Troise, and G. De Natale (2014), The volcanic and geothermally active Campi Flegrei caldera: An integrated multidisciplinary image of its buried structure, *Int. J. Earth Sci.*, *103*(2), 401–421.

Prudencio, J., J. M. Ibáñez, A. García-Yeguas, E. Del Pezzo, and A. M. Posadas (2013), Spatial distribution of intrinsic and scattering seismic attenuation in active volcanic islands-II: Deception island images, *Geophys. J. Int.*, *195*(3), 1957–1969.

Prudencio, J., E. Del Pezzo, J. Ibáñez, E. Giampiccolo, and D. Patané (2015a), Two-dimensional seismic attenuation images of Stromboli Island using active data, *Geophys. Res. Lett.*, *42*, 1717–1724, doi:10.1002/2015GL063293.

Prudencio, J., J. Ibáñez, E. Del Pezzo, J. Martí, A. García-Yeguas, and L. De Siena (2015b), 3D attenuation tomography of the volcanic island of Tenerife (Canary Islands), *Surv. Geophys.*, *36*(5), 693–716, doi:10.1007/s10712-015-9333-3.

Sato, H., M. C. Fehler, and T. Maeda (2012), *Seismic Wave Propagation and Scattering in the Heterogeneous Earth: Second Edition*, 494 pp., Springer, New York.

Selva, J., G. Orsi, M. A. Di Vito, W. Marzocchi, and L. Sandri (2012), Probability hazard map for future vent opening at the Campi Flegrei caldera, Italy, *Bull. Volcanol.*, *74*(2), 497–510.

Serlenga, V., S. Lorenzo, G. Russo, O. Amoroso, S. Garambois, J. Virieux, and A. Zollo (2016), A three-dimensional QP imaging of the shallowest subsurface of Campi Flegrei offshore caldera, southern Italy, *Geophys. Res. Lett.*, *43*, 209–218, doi:10.1002/2016GL071140.

Todesco, M., A. Rinaldi, and M. Bonafede (2010), Modeling of unrest signals in heterogeneous hydrothermal systems, *J. Geophys. Res.*, *115*, B09213, doi:10.1029/2010JB007474.

Todesco, M., A. Costa, A. Comastri, F. Colleoni, G. Spada, and F. Quareni (2014), Vertical ground displacement at Campi Flegrei (Italy) in the fifth century: Rapid subsidence driven by pore pressure drop, *Geophys. Res. Lett.*, *41*, 1471–1478, doi:10.1002/2013GL059083.

Vanorio, T., and W. Kanitpanyacharoen (2015), Rock physics of fibrous rocks akin to Roman concrete explains uplifts at Campi Flegrei Caldera, *Science*, *349*(6248), 617–621.

Vanorio, T., J. Virieux, P. Capuano, and G. Russo (2005), Three-dimensional tomography from *P* wave and *S* wave microearthquake travel times and rock physics characterization of the Campi Flegrei Caldera, *J. Geophys. Res.*, *110*, B03201, doi:10.1029/2004JB003102.

Vilardo, G., G. Ventura, E. Bellucci Sessa, and C. Terranova (2013), Morphometry of the Campi Flegrei caldera (southern Italy), *J. Maps*, *9*(4), 635–640.

Woo, J. Y., and C. R. Kilburn (2010), Intrusion and deformation at Campi Flegrei, southern Italy: Sills, dikes, and regional extension, *J. Geophys. Res.*, *115*, B12210, doi:10.1029/2009JB006913.